Further Exploration of Regional-Class Hybrid Wing-Body Aircraft Through Multifidelity Optimization

Aiden G. Lee *, Thomas A. Reist † and David W. Zingg ‡
University of Toronto Institute for Aerospace Studies,
4925 Dufferin St., Toronto, Ontario, M3H 5T6, Canada

Regional-class hybrid wing-body (HWB) aircraft that satisfy various stability and control requirements are optimized for a combination of cruise drag and maximum takeoff weight by using a multifidelity multidisciplinary optimization framework based on solutions to the Reynolds-averaged Navier-Stokes equations. The design mission consists of flying 100 passengers a distance of 2 000 NM (3 704 km) at an altitude of 36 000 ft (10 973 m) and a speed of Mach 0.78. HWB aircraft that meet these requirements were previously optimized while ensuring they satisfy static margin and trim requirements at cruise, achieve directional trim with one engine inoperative on the ground using winglet-mounted rudders, and satisfy a rotation constraint using nearly full-span pitch effectors (Reist, T.A., et al., J. of Aircraft, Vol. 56, 2019). However, the rotation constraint is significantly detrimental to performance, and the resulting aircraft are highly unstable at low speeds. The present study addresses the former issue by allowing a lower pitch control margin to saturation and the latter issue by constraining the low-speed trimmed static margin. The geometric flexibility given to the optimizer is then increased. First, the placement and orientation of the polyhedron enclosing the cockpit, cabin, and cargo holds is optimized simultaneously with the geometry while also modeling telescoping nose landing gear to ease the burden of achieving rotation. Second, local shape control is increased through a more refined geometry control system. Through these means and a few other model improvements, an HWB aircraft is found that satisfies the additional low-speed constraints and has a cruise lift-to-drag ratio of 22.8, leading to 15.7% lower cruise drag and 11.2% lower fuel burn for the design mission relative to the previously optimized aircraft.

I. Nomenclature

Acronyms

CG	=	Center of gravity
FFD	=	Free-form deformation
HWB	=	Hybrid wing-body
HWB100-nN$_{\text{modifications}}$	=	Case identifier: 100-passenger Hybrid wing-body aircraft optimized while considering n analysis points and a narrow (N) cabin layout (7-abreast, 2-3-2) and with specified modifications to the baseline problem definition
MLG, NLG	=	Main landing gear, nose landing gear
MTOW, OEW, OEW + MFW, MZFW	=	Loading conditions: maximum takeoff weight, operating empty weight, maximum fuel weight onboard, and maximum zero-fuel weight
OEI	=	One engine inoperative
OML	=	Outer mold line
RANS	=	Reynold-averged Navier Stokes
S&C	=	Stability and control
SNOPT	=	Sparse nonlinear optimizer

*PhD Student; aiden.lee@mail.utoronto.ca
†Research Associate; tom.reist@utoronto.ca
‡University of Toronto Distinguished Professor of Computational Aerodynamics and Sustainable Aviation; Director, Centre for Research in Sustainable Aviation; Director, Centre for Computational Science and Engineering; AIAA Associate Fellow; dwz@utias.utoronto.ca

Variables

b	=	Wingspan
c	=	Chord length
c_l	=	Sectional lift coefficient
C_L	=	Aircraft lift coefficient
C_m	=	Aircraft pitching moment coefficient
$I_{yy}^{(G)}$	=	Mass moment of inertia with respect to the CG
$\mathcal{J}$	=	Objective function
K_n	=	Longitudinal static margin
l_{ref}	=	Reference length equal to the mean aerodynamic chord of the baseline shape, i.e. 12.9 m
L, D, T, W	=	Lift, drag, thrust, weight
m	=	Mass
S	=	Planform area
x, y, z	=	Cartesian coordinates
α	=	Aircraft angle of attack; $\alpha = 0°$ is defined when the cabin lies flat
$\Delta\{\cdot\}$	=	Change in the variable $\{\cdot\}$
$\ddot{\theta}$	=	Pitch acceleration
μ	=	Rolling coefficient of friction
θ_c	=	Cabin deck angle

Common Scripts

$\{\cdot\}_c$	=	Pertains to the cabin of the aircraft
$\{\cdot\}_{ref}$	=	Reference value

II. Introduction

Airframe and propulsion technologies have both significantly improved with each new generation of transport aircraft, but a step-change in the former is required to meet ambitious industry goals, such as a 50% reduction in fuel burn by 2050 relative to 2005 levels [1]. Hence, the pursuit of revolutionary rather that evolutionary changes will soon be the preferred way forward. Research on unconventional aircraft has produced promising novel configurations, namely the truss-braced-wing, the box-wing, the hybrid or blended wing-body (HWB or BWB), and the double-bubble [2, 3]. The flying-V configuration was also recently introduced [4].

The HWB is an unconventional aircraft configuration that was first conceptualized around 1988 [5]. Many years of research that resulted in the Boeing BWB-450 aircraft concept were summarized by Liebeck in a 2004 publication [6]. The novel configuration typically offers a relatively high wetted aspect ratio for a given internal volume. This characteristic is recognized as its principal inherent aerodynamic advantage over conventional tube-and-wing aircraft. Other significant advantages are discussed in Ref. [6]. Results from conceptual design projects worldwide have since corroborated the superior fuel efficiency of the HWB configuration [7]. For instance, a widebody-class HWB aircraft that could enter into service around 2035 was shown to burn 54% less fuel than the Boeing 777-200LR baseline aircraft, where about half of this reduction is due to its superior aerodynamic efficiency [2]. More recently, Airbus has unveiled its MAVERIC flight demonstrator aircraft. Aerodynamic efficiency is expected to result in a 20% fuel savings over a modern single-aisle-class aircraft [8].

Numerical optimization frameworks based on high-fidelity flow models are well-suited to design the multifunctional aerodynamic surfaces required to create practical HWB aircraft; see, for example, Refs. [9–12]. Stability and control (S&C) constraints have been enforced in such contexts. For instance, Méheut et al. [12] performed aerodynamic shape optimization of the AVECA HWB while enforcing cruise trim constraints and ensuring rotation was achievable through a low-speed pitching moment constraint. Cruise performance was found to be unaffected by the latter S&C constraint. A longitudinal dynamic stability constraint was included in an Euler equation-based aerodynamic shape optimization framework by Mader and Martins [13]. Optimally swept wings were required in addition to section shape design variables to satisfy the constraint at higher transonic speeds. However, since it requires computations approximately 15

times as expensive as a steady flow evaluation, such a constraint may only be warranted in advanced stages of design. Besides, the wings of HWB aircraft are generally swept to satisfy, for instance, a static margin constraints for a more modest cost of only 2 flow solutions [14], or simply to minimize wave drag. Lyu et al. [15] successfully imposed trim, static margin, center of gravity (CG) location, and centerline bending moment constraints in the multipoint aerodynamic shape optimization of the Boeing BWB-450 based on the Reynolds-averaged Navier-Stokes (RANS) equations. Finally, Reist et al. [14] studied the impact of several simultaneously enforced S&C requirements on the optimal shape of regional-class HWB aircraft. In that study, the aircraft was trimmed and its static margin was limited at cruise, directional trim was achieved on the ground with one engine inoperative using rudders, and nearly full-span pitch effectors were sized to ensure sufficient control authority to initiate rotation during the takeoff ground-run. All constraints were satisfied, but the rotation constraint was shown to lead to significant penalties in both drag and weight.

Some low-speed S&C requirements pose a challenge for HWB aircraft, as they lack an empennage. Accordingly, considerable work has been done to study this aspect of their design, in addition to that reported in Ref. [14]. For instance, the requirement of directional control authority at low speed was found to be particularly challenging for the X-48B HWB aircraft despite its use of both winglet-mounted rudders and outboard split elevons [16]. Cook and de Castro [17] studied both the static and dynamic S&C characteristics of a large HWB aircraft. The limited static-margin range in which longitudinal trim can be achieved at low speed was demonstrated. Garmendia et al. [18] compared a number of trailing-edge control surface layouts, combining between 7 and 11 of them in several arrangements. A reduction in weight, actuator power usage, and fuel burn was achieved by combining adjacent elevons into larger control surfaces of unequal span fractions.

Despite ample interest in the HWB concept [6, 12, 16, 19–22], relatively few projects have focused on regional- or single-aisle-class airliners, likely because there is some doubt that the HWB configuration is advantageous for small aircraft; see, for example, Ref. [2]. After finding that the classical wide HWB planform is suboptimal for regional-class aircraft, Reist and Zingg used exploratory aerodynamic shape optimization based on the RANS equations to develop the more slender and efficient *lifting fuselage configuration* [23]. Another notable example is the work of DZYNE Technologies [24]. Their regional-class HWB burns 29% less fuel due to improved aerodynamics alone compared to the Embraer E190 baseline aircraft. Telescoping landing gear was deemed a key enabling technology that decouples rotation ability from performance at other stages of flight. That exact dependency severely impacted the cruise performance of the optimized aircraft reported in Ref. [14], making them significantly heavier, and contributing to their excessive low-speed longitudinal static instability.

The study by Reist et al. [14] provides the starting point for the current investigation, which is driven by the following two objectives: 1) To further investigate the impact of S&C requirements on the optimal shape and performance of regional-class HWB aircraft and 2) To provide an improved estimate of their potential fuel-efficiency through a methodical expansion of the design space aimed at mitigating the punitive effect of the S&C requirements. To these ends, regional-class HWB aircraft are optimized using a RANS-equation-based multifidelity multidisciplinary optimization framework. The design mission consists of flying 100 passengers a distance of 2 000 NM (3 704 km) at an altitude of 36 000 ft (10 973 m) and a speed of Mach 0.78. The optimizer is given significant freedom to determine the span and the sweep and dihedral angles of each major aircraft section, in addition to local twist angles, chord lengths, and cross-section thicknesses.

Following the overview of the optimization framework and the problem definition given in Sections III and IV, respectively, Section V presents the effect on performance of constraining the low-speed trimmed static margin. The sensitivity of the resulting design to the pitch effector deflection angle limits is discussed in Section VI. Then, telescoping nose landing gear (NLG) is included in the analysis and the aircraft is shaped around an optimally positioned cabin; the implications of these choices are discussed in Section VII. Finally, Section VIII discusses the effect on performance of a refined local control of the geometry, and conclusions are presented in Section IX.

III. General Overview of the Optimization Framework

The multifidelity multidisciplinary optimization algorithm called Jetstream is described in this section. HWB-specific applications of a version of the algorithm are those of Kuntawala et al [11], Reist and Zingg [23], and Reist et al. [14]. Moreover, Koo and Zingg [25] used Jetstream to investigate various nonplanar and nonlinearly tapering wing systems.

A. Geometry Parameterization and Control and Integrated Mesh Deformation

Jetstream defines aircraft shapes using stitched B-spline surfaces that are analytically deformed through their control points. An overarching free-form and axial deformation geometry control system developed by Gagnon and Zingg [26]

is used to achieve shape control in this work. To set up the first level of the geometry control system, a set of joined axial curves, which are B-spline curves of sufficient order and with a desired control point density, are first placed along the quarter-chord of the wing-body. The B-spline surface control points are then embedded inside a set of free-form deformation (FFD) volumes (B-spline volumes) that comprise several streamwise-aligned cross-sections of control points. These *control stations* are fixed at a constant parametric location on an axial curve. Global shape control is achieved by manipulating the axial curve control points, while local control is provided through manipulation of the FFD volume control points.

To integrate the mesh deformation algorithm of Hicken and Zingg [27] with the geometry control system, mesh nodes are first assigned a parametric location within a B-spline volume; there exists one per block of the multiblock structured mesh. The B-spline volume control points mimic a coarse mesh and thus can be used to deform the computational mesh through an inexpensive yet robust method. To initiate a mesh deformation, a perturbation in the B-spline surfaces that define the OML is propagated throughout the control point mesh via the linear elasticity equations with prescribed-displacement boundary conditions. The computational mesh is then algebraically reconstructed based on the parametric location of its nodes.

The modeling of trailing edge control surfaces is performed using the method developed and validated by Reist et al. [14]. A control surface is deflected by rotating a fraction of the FFD volume control points of several adjacent control stations through a specified deflection angle about a nearby straight hinge line.

B. RANS Flow Solver and Spatial Discretization

Clean airframe drag is calculated by a parallel implicit solver for the RANS equations closed with the negative variant of the Spalart-Allmaras turbulence model that was validated during the 5$^{\text{th}}$ AIAA Drag Prediction Workshop [28, 29]. Second-order summation-by-parts operators are used for spatial discretization, and simultaneous approximation terms impose boundary and block interface conditions. The generalized minimal residual (GMRES) Krylov subspace method is used with approximate Schur preconditioning in an inexact Newton method for the solution of the linearized discrete equations at every flow solver iteration.

The same relatively coarse multiblock structured meshes used in Ref. [14] are reused in this work. They comprise approximately 2.4×10^6 nodes. For operations in ground effect, flow tangency boundary conditions and a prescribed velocity equal to the ground-speed are imposed at a ground plane on a modified grid. These grids effectively balance accuracy and computational cost, while predicting with reasonable accuracy the relative contributions of pressure and friction drag to the total clean-airframe drag. In addition, the aerodynamic force and moment correction factors developed for similar HWB aircraft shapes at the same operating conditions in Ref. [14] are reused to approximate grid-converged values to obtain a more accurate estimate of the fuel load. All aerodynamic quantities reported in this paper are based on corrected coarse-grid values.

C. Conceptual-Level Aircraft Design Toolbox

Conceptual-level aircraft design relations are used to calculate many aspects crucial to multidisciplinary design optimization. Although details have been omitted for brevity, they can be found in Ref. [14]. Excrescence drag, nacelle drag, and windmilling drag, are obtained through low-fidelity models and added to the (corrected) clean-airframe drag, but nacelle-OML interactions are ignored at this stage. Two engines are sized to produce a rate of climb of 300 ft/min (1.52 m/s) at the top of climb. No assumptions are made about reliance on future technology levels.

The structural, fixed, and fuel weights are also estimated using conceptual-level relations at every design iteration. A fixed weight of 24 000 lb (10 886 kg), which includes that of the landing gear, hydraulics and operational items, is assumed to be independent of the design variables. Note that the wing weight model used is that of Torenbeek [30], and it is dependent on span, area, and sweep angle; see Ref. [14] for additional modeling details. The balance diagram comprises four corners where the aircraft weight and CG are measured at maximum takeoff weight (MTOW: airframe, full passenger payload, and fuel for the design mission), operating empty weight (OEW: airframe only), maximum fuel weight (OEW + MFW: airframe and full fuel tanks), and maximum zero fuel weight (MZFW: airframe and full passenger payload).

The CG and mass moment of inertia about the lateral axis are calculated based on a few assumptions. Namely, it is assumed that the structural mass distribution is homogeneous within the shell of the airframe. Hence, the weight of the centerbody, wings, and winglets acts through their respective shell centroids. However, the resulting structural CG is allowed to be perturbed by up to 15% to account for strategic placement of heavy components during more advanced stages of design. The fuel CG is assumed to lie at the volume centroid of the wings, the payload weight acts at the

volume centroid of the polyhedron enclosing the cockpit, cabin, and cargo holds, the fixed weight acts through the shell centroid of the centerbody, and the weight of the two engines acts one nacelle diameter upstream of the centerline trailing-edge. The engines are laterally offset by one nacelle diameter from the centerline, and are placed one-and-a-half nacelle diameters above the centerline chord line.

Finally, the main landing gear (MLG) axles are longitudinally and vertically positioned where a line drawn downwards at 10° from the aftmost CG (perturbed aft by 1% l_{ref}) intersects a horizontal plane at the height of the MLG axles. The MLG is laterally positioned 2 ft outboard of the cargo holds. Its location influences some on-ground constraints that are introduced in Section IV.E. For some of the cases presented herein, the relative positioning of the MLG with respect to the aftmost CG accounts for the use of telescoping NLG; see Section VII.

D. Gradient-Based Optimization Algorithm and Flow-Dependent Gradient Evaluation

The sparse nonlinear optimizer (SNOPT) gradient-based optimization algorithm is used as it is able to efficiently solve large-scale constrained problems. The high cost of evaluating the flow-dependent objective function and constraints motivates the use of a gradient-based algorithm. The optimizer uses sequential quadratic programming and approximates Hessian matrices with the method of Broyden, Fletcher, Goldfarb, and Shanno. The algorithm is further described in Ref. [31].

Accurate gradients are required to acceptably converge the optimization problem. Due to the large number of design variables, flow-dependent gradients are evaluated using the efficient discrete adjoint method. A simplified and flexible version of the generalized conjugate residual with orthogonalization and truncation (GCROT) algorithm [32] is used to efficiently solve an adjoint system to a tolerance of 10^{-8} in about one-third of the time required for a flow solution. Details pertaining to the implementation of the discrete-adjoint method within Jetstream are given in Refs. [26, 27, 33].

IV. Optimization Problem Formulation

A. Design Mission

As in Ref. [14], the regional-class HWB aircraft being optimized must transport a full passenger payload of 100 passengers, or 22 500 lb (10 206 kg), a nominal distance of 2 000 NM (3 704 km) while cruising at 36 000 ft (10 973 m). Although there is evidence that HWB aircraft attain a more favorable balance between zero-lift drag and lift-dependent drag at higher cruise altitudes due to their relatively large surface area [23], some arguments can be made against such a practice. Namely, the additional fuel required for climbing may not be justified for some regional missions, the weight penalty resulting from a cabin able to resist higher pressure differentials detracts from this advantage (and is not captured by the current algorithm), and the impact of nitrogen oxides from aircraft engines worsens with altitude [34]. Consequently, optimizing regional-class HWB aircraft under the chosen conditions seems appropriate and it will enable a fairer comparison to be made with existing conventional tube-and-wing aircraft in future studies. However, a future study to determine an optimal cruise altitude may be warranted, as low nitrogen oxide combustors [34] or advanced composite structural solutions [35] could be employed if these technologies reach a sufficient level of maturity concurrently with the development of HWB aircraft.

B. Baseline and Initial Shapes

Jetstream uses a baseline shape to generate the initial FFD volumes and axial curves that are perturbed by the geometric design variables – see Section IV.D. The mean aerodynamic chord of the baseline shape is $l_{\text{ref}} = 12.9$ m; this value is used to nondimensionalize various quantities. Although an optimization can be started from the baseline shape, any suitable shape can be used instead to accelerate convergence. In this paper, it consists of a partially optimized result, shown in Fig. 1a, that satisfies many S&C constraints and is shock-free at the design cruise conditions. The shape is controlled by manipulating 10 axial curve control points distributed between 4 axial curves on each side of the aircraft. One FFD volume is driven by each axial curve, and there exists one axial curve for each main section on the aircraft, i.e. the half-centerbody, transition region, wing, and winglet. Each control station, of which there exist 25 on each side of the aircraft, comprises 22 control points (11 on the top and 11 on the bottom of the FFD volume). On the left-hand side of Fig. 1a, the polyhedron enclosing the cockpit, cabin, and cargo holds is shown. These are not directly affected by axial and free-form deformation, but the aircraft must be designed around them.

In Refs. [14] and [23], it was confirmed that a narrow cabin layout improves the performance of regional-class HWB aircraft. Consequently, the seven-abreast cabin with a 2-3-2 seating arrangement shown in Fig. 1b is used. Lower

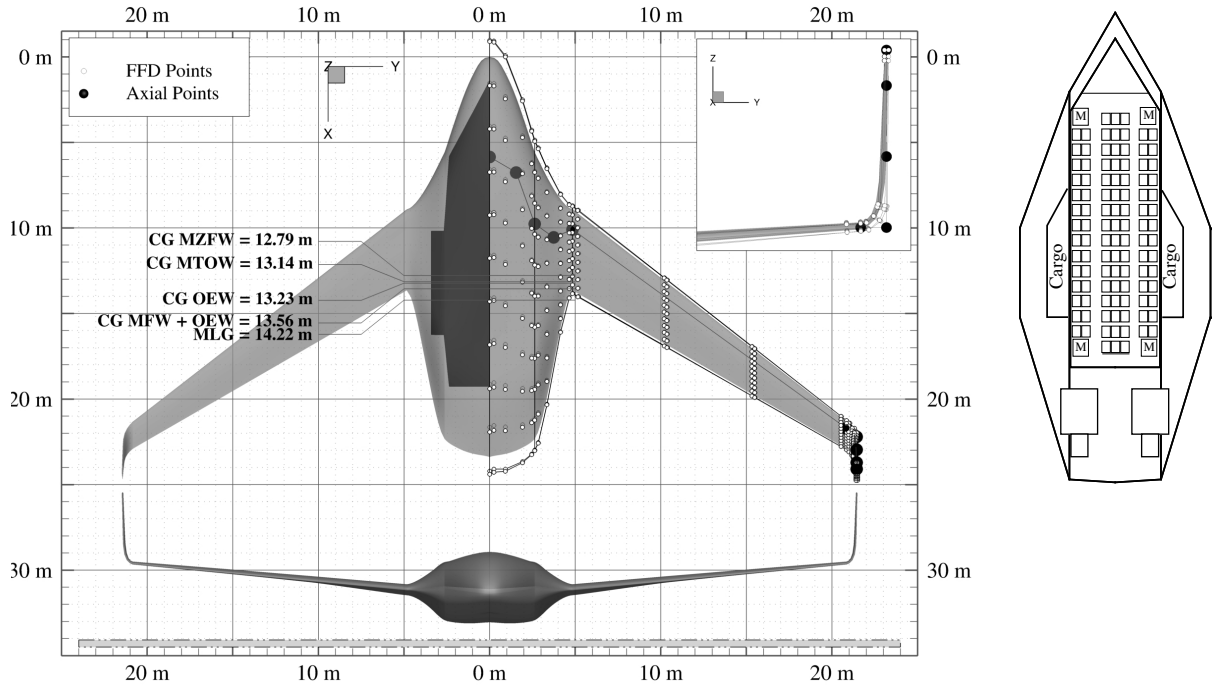

(a) Initial geometry and geometry control system; Inset: winglet detail **(b) Cabin layout**

Fig. 1 General initialization details

centerbody weight and surface area, and thus lower total drag, typically result from this choice. In addition, these narrower HWB aircraft tend to operate more efficiently than their counterparts with wider cabins when cruising at the chosen altitude because a more favorable balance between zero-lift drag and lift-dependent drag is achieved. A future study could ascertain the optimal cabin layout, but the presence of two aisles has a positive impact on boarding and egress times.

One centerbody elevator, six wing-mounted elevons of equal length, and two winglet mounted rudders are defined. The elevator covers 10% of the local chord and it spans the centerbody. The elevons, which cover 30% of the local chord, collectively span 96% of the wing. The slender cabin layout is consistent with the need to elongate the aft centerbody for the purpose of increasing the moment arm of its elevator in order to achieve rotation. Two rudders span approximately 80% of the vertical section of the winglet and they cover 30% of the local chord.

C. Objective Function

The objective function consists of a normalized equally-weighted sum of drag at the start of cruise and MTOW, as used in Ref. [14]. The reference values were obtained by performing trim-constrained single-point drag minimization on the baseline shape. Fuel burn can be reduced by minimizing drag, but manufacturing and operating costs depend on MTOW. The objective function is mathematically expressed as:

$$\mathcal{J} = \frac{1}{2}\frac{W_{\text{MTOW}}}{W_{\text{MTOW}_{\text{ref}}}} + \frac{1}{2}\frac{D_{\text{start of cruise}}}{D_{\text{start of cruise}_{\text{ref}}}}$$

Note that, due to the high computational cost of these problems, convergence is called when all constraints are satisfied and the SNOPT merit function drops only in the fifth significant digit between iterations instead of when the optimality tolerance of 10^{-4} is reached. Nonetheless, optimality is of order 10^{-4} at convergence.

D. Design Variables and Linear Constraints

The axial curve design variables control the span and the sweep and dihedral angles of each major section of the aircraft. For instance, the span and quarter-chord sweep angle of the wing are designed through the displacement of the

two wing axial curve control points in the xy-plane. The wingtip moves out-of-plane to design the dihedral angle. The winglet is built by bending its axial curve out-of-plane, as shown in the inset of Fig. 1a.

The sectional design variables locally control the twist angle, chord length, and section shape. The twist angle is designed by rotating a control station about the axial curve. The chord length is varied through the chordwise scaling of a control station. Finally, the section shape is controlled by displacing the FFD volume control points along the local vertical direction, which is reoriented as a function of the twist angle.

The axial curve and sectional design variables are collectively known as the geometric design variables. Linear constraints on many geometric design variables are initially used to accelerate convergence and keep manufacturing costs relatively low. Twist angles are interpolated between the root and the tip of each FFD volume, and so are chord lengths except on the centerbody. Section shapes are similarly interpolated except on the wing, where they are free to be designed at elevon edges. The characteristic initial blending of the centerbody, transition region, and wing is conserved by interpolating the displacement of the middle axial curve control points of the centerbody and transition region.

Some sectional design variable bounds are active at a solution. Namely, the chord length at the wingtip must be at least 5 ft (1.52 m) to enable proper winglet mounting, and the winglet must have a tip chord of at least 3 ft (0.914 m) to house rudder hardware. Given the simplicity of the structural model used to size the wings, the local thickness-to-chord ratios must not shrink to less than 80% of their original values; this factor is 50% on the thicker centerbody and transition region.

The deflection angles of the centerbody elevator, 6 elevons, and 2 rudders are also design variables at some analysis points – see Section IV.E.2 and Appendix A for their description. The pitch effectors can deflect only a fraction of the 25° limit for pitch control, as a sufficient control margin must be maintained in flight. However, the rudders can be fully deflected (30°) to achieve directional trim in the critical situation where one engine fails on the ground.

The angle of attack at cruise is also a design variable. It is limited such that the deck angle satisfies $-2.5° \leq \theta_c \leq 2.5°$ knowing that the cabin lies flat when the aircraft is on the ground (except when telescoping landing gear is used, see Section VII). The angle of attack at the low-speed analysis point is variable but unbounded. In summary, the baseline case presented in Section V has 170 effective design variables.

E. Nonlinear Constraints and Required Analysis Points

1. Nonlinear Geometric Constraints

The following nonlinear geometric constraints are imposed: 1) An acceptable range of near-ground pitch and roll attitudes is maintained through a constraint that prevents tip-strikes up to 9° and 9.5°, respectively. 2) When this constrains the position of the wingtip, the dihedral angle is limited to 4° to prevent excessively long wings from being designed. 3) Ground clearance is maintained during the takeoff ground-run by ensuring that all points on the aircraft are located at least 3 ft (0.914 m) above the ground. 4) The fraction of the wing volume that can store fuel is calculated by multiplying the wing OML volume by a factor to account for the volume of the wing box, which is assumed to lie between 20% and 70% of the local chord, together with a utilization factor to account for the usable volume within the wing box. In addition, no fuel is stored within 5 ft (1.52 m) of the base of the winglet as per lightning strike requirements. As a result, 57.6% of the wing OML volume can store fuel. 5) The section of the polyhedron enclosing the cabin and cockpit must reside within the OML of the centerbody, thus acting as the main driver of its shape. The cargo holds can reside within the transition region. 6) The centerbody span must be greater than the cabin width so that the centerbody weight model functions as intended. 7) The winglet aspect ratio must not exceed 4. This constraint acts as a proxy for its structural integrity when combined with appropriate thickness constraints because the winglet weight model is based solely on wetted area. 8) The hinge line of the (single) centerbody elevator is constrained to be perpendicular to the symmetry plane.

2. Trim, Stability, and Control Constraints and Required Analysis Points

The aircraft must be trimmed at cruise with the CG at the design point and at low speed with the aftmost CG. The static margin is also constrained at cruise and at low speed through the following finite difference approximation: $K_n \approx -\Delta C_m/\Delta C_L \geq -4\%\ l_{\text{ref}}$, where the aerodynamic derivatives are approximated by perturbing the angle of attack by 0.1°. A negative lower bound was used because a slightly unstable aircraft augmented with an adequate control system will likely be certifiable by the time HWBs can be expected to enter into service. Note that the static margin at cruise is evaluated at the design point, but it is then adjusted to account for the position of the aftmost CG relative to the cruise CG. Such an approach is approximate, as trimming for an aft CG typically further destabilizes these HWB

aircraft [14], but the constraint is far from active in all cases. Moreover, post-optimization checks have confirmed that the effect of trim is indeed negligible at this analysis point. The trimmed low-speed static margin is directly evaluated at the aftmost CG. This constraint is always active and typically more sensitive to trimming.

The preceding discussion justifies two out of the four analysis points, namely the start of the cruise segment of the design mission and low-speed flight. The data at the start of cruise are used to calculate the drag component of the objective function, engine size, fuel loads, and structural weights. At the low-speed analysis point, it is assumed that the loading condition corresponds to an aft CG, i.e. when the aircraft is at OEW + MFW. A few destabilizing factors combine to make this loading condition critical: It typically corresponds to the aftmost CG and it requires substantial downward pitch effector deflections and a high angle of attack to trim. This off-design analysis point was added after considering one impractical mechanism designed by the optimizer to satisfy the cruise static margin constraint in Ref. [14]: Local section shape tailoring near the wingtip produced a steep but isentropic pressure recovery on the top surface of the wing. The aerodynamic centers of these sections, and therefore the neutral point, were thus moved rearward but only in the transonic conditions of cruising flight. Consequently, the static margin was decreased to far below acceptable levels at low speed.

Another off-design analysis point determines the size, shape, and position of the winglets such that rudders allow directional trim with one engine inoperative at a desired minimum control speed on the ground. This analysis point is static, however, so it is in fact a proxy for the true time-dependent test for minimum control speed on the ground that also considers pilot response. However, the selected speed is lower than the minimum control speed in the air, and zero bank angle must be maintained, so this is nonetheless a more critical constraint. Note that the NLG is conservatively assumed to be unloaded because any lateral force produced would oppose the yawing moment created by the operating engine, and that ground effect is modeled as described in Section III.C.

The last off-design analysis point models the start of rotation. This analysis point impacts the size, shape, and position of the wings and the centerbody as the pitch effectors that they house must be able to initiate rotation. Conservatively perturbed CGs are used at both on-ground analysis points to account for potential variations in aircraft loading. A variation on a dynamical model given by Roskam [36] for conceptual-level takeoff analysis was developed to ensure that a minimum pitch acceleration of $3\,\mathrm{deg/s^2}$ is attainable at the instant that rotation is initiated. It differs in that it accounts for the vertical acceleration of the CG during the motion. Neglecting this admittedly small value results in an overestimation of the effective mass moment of inertia, with the new value being given by $I_{yy}^{(G)} + m\bar{x}(\bar{x} - \mu\bar{z})$ as opposed to $I_{yy}^{(G)} + m(\bar{x}^2 + \bar{z}^2)$. Note that $\bar{x}$ and $\bar{y}$ locate the CG from a reference frame positioned at the MLG ground-contact point. The rotation constraint is evaluated for all four loading conditions to ensure that the most critical but consistent combination of weight, CG, and mass moment of inertia constrains the design. Like the directional trim constraint, the rotation constraint is also evaluated in ground effect to capture the corresponding changes in aerodynamic forces and moments.

V. Baseline Problem and Variants

The baseline problem is known as Case HWB100-4N, or just 4N for short. Other than the addition of the low-speed trim and static margin constraints, this problem differs from that solved by Reist et al. [14] in the following respects:

1. The structural CG is located at the shell centroid of the OML as opposed to its volume centroid, and its mass moment of inertia also reflects the distribution of mass throughout a shell.
2. The calculated structural CG can be perturbed by ±15% to account for strategic choices in more advanced stages of design.
3. The improved dynamical modeling of the start of rotation described in Section IV.E.2 is used.
4. Instead of limiting the deflection angle of every pitch effector to 33% of that produced by a full actuator extension, as in Ref. [14], the elevons can deflect up to 50% and the elevator can deflect up to 80%.
5. The cabin is made to lie flat during the takeoff ground-run instead of 2° nose-up, and telecoping landing gear is modeled explicitly in a later case – see Section VII.

In Ref. [14], the pitch effector deflection angle limit was only 33% of the 25° limit, but it can be argued that most HWB aircraft with nearly full-span pitch effectors can easily remain controllable even if higher deflection angles were used when needed, such as during rotation (low-speed trim is achieved without every pitch effector reaching its deflection angle limit, as described later in this section). Besides, angular motion in flight occurs about the CG as opposed to the MLG axles, so the moment arm of most pitch effectors is increased. In addition, the effective mass moment of

Table 1 Characteristics and performance of optimal shapes

	3N	4N	$4N_{(R)}$	$4N_B$	$4N_C$
Performance data *					
Cruise drag [kN]	20.29	20.75	19.99	20.04	19.45
Cruise drag coefficient [counts]	81.54	82.48	88.35	84.95	86.77
MTOW [kg]	48 600	49 000	46 600	47 400	46 700
Block fuel burn [kg]	7 040	7 160	6 880	6 920	6 770
Cruise L/D	22.75	22.44	22.15	22.49	22.83
Cruise K_n, aft CG [% l_{ref}]	**-4.00**	-1.38	-0.778	-1.34	-1.37
Low-speed K_n [% l_{ref}]	N/A	**-4.00**	**-4.00**	**-4.00**	**-4.00**
Key geometric data *					
Span [m]	41.39	43.98	34.12	38.06	37.05
Planform area [m^2]	255.3	258.1	232.1	241.9	230.0
Wetted area [m^2]	584.2	593.4	543.0	562.3	542.4
Wetted aspect ratio	2.932	3.260	2.144	2.577	2.531
Cruise deck angle [deg]	1.38	1.53	**2.50**	**2.50**	**2.50**
Tip-strike margin [m]	**0.00**	**0.00**	0.772	1.38	1.52

* Boldface indicates constraint activity.

inertia is decreased. These reasons motivate the use of an elevon deflection angle limit of 50%. The higher 80% limit for the elevator was chosen based on the sensitivity study described in Section VI, where it is shown that substantial performance and weight benefits can thus be obtained.

In light of the model improvements listed above, and in order to ascertain the mechanisms favored by the optimizer to satisfy the low-speed S&C constraints, the problem originally solved by Reist et al. [14] was rerun. It excludes the low-speed trim and static margin constraints and is known as Case 3N. A variation on Case 4N where the rotation constraint was not imposed, referred to as Case $4N_{(R)}$, was also solved to ascertain the mechanisms favored by the optimizer to supplement the pitching moment at the start of rotation after having made full use of the pitch effectors. For ease of comparison, Table 1 contains results from this section as well as those from Sections VII and VIII. Additional results can be found in Table 2 in Appendix B.

Trim is achieved at low speed in Cases 4N and $4N_{(R)}$ through deflecting the elevator downward by the full 80% (20°), but the elevons are not fully utilized. For instance, Model 4N trims at low speed with its inboard elevon deflected downward by 4.29°, its middle elevon deflected upward by 1.39°, and its outboard elevon deflected downward by 0.61°. The low-speed trim problem is underdetermined, and the low-speed static margin constraint is active in both cases, so pitch effector deflection angles are selected such that the static margin is maximized. This is true of all cases presented in this paper that include the corresponding low-speed constraints.

When compared to the original result reported in Ref. [14], Model 3N performs markedly better. Cruise drag is reduced by 12.1%, MTOW is 1.5% lower, and block fuel burn is reduced by 8.5%. These improvements are due to items 1 through 4 in the list above; item 5 has a detrimental effect but it is necessary that the cabin lie flat at the gate. The wing section shape tailoring that was highlighted in Ref. [14] did not arise in Model 3N. There, shape tailoring was used by the optimizer as one means of satisfying the (high-speed) static margin constraint once planform freedom was exhausted or driven by other constraints. The absence of wing section shape tailoring in these results is due in large part to the increased deflection angle limits and the structural CG perturbation design variable. However, like the aircraft obtained in Ref. [14], Model 3N is also highly unstable at low speed, as evidenced by the penalty paid to increase the low-speed static margin to its target value. It amounts to 2.3% in cruise drag, 0.82% in MTOW and 1.7% in block fuel burn. Major geometric differences between Models 3N and 4N include a different wing planform, as can be seen by comparing Figs. 2 and 3. Among the geometric differences, those that help stabilize the aircraft include an 0.543 m aft displacement of the wing roots, a higher taper ratio (0.407 vs. 0.356), and increased washout (2.63° vs. 1.69°).

The data also show that, even while using an 80%-deflected elevator and 50% deflected elevons, Model 4N suffers

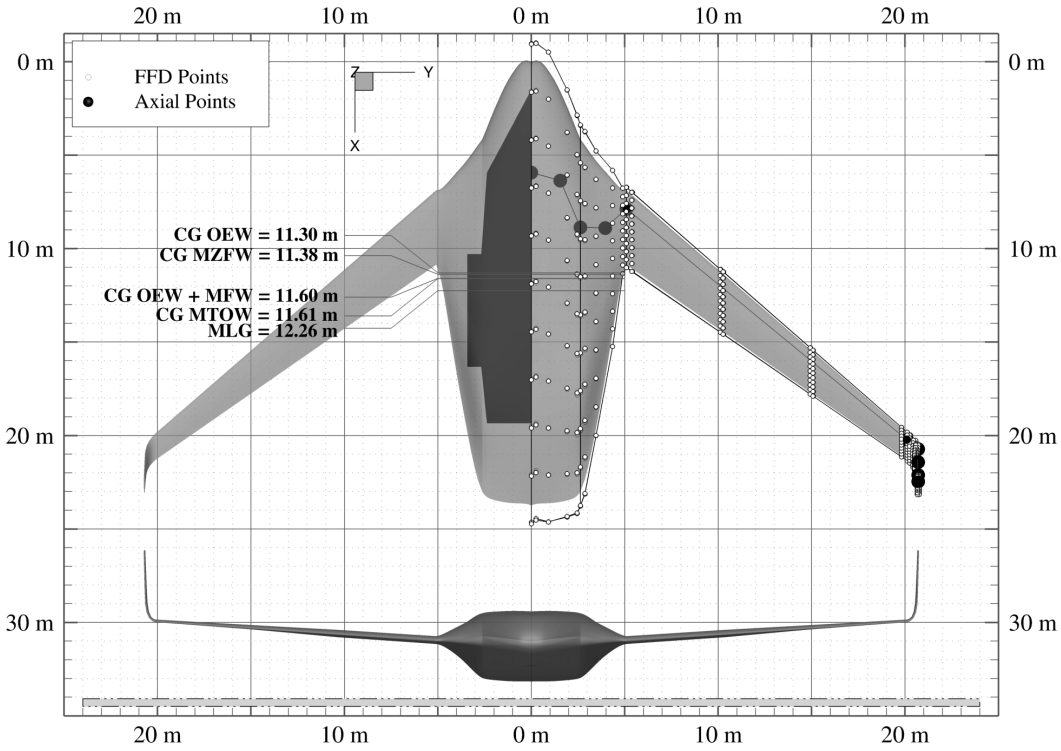

Fig. 2 Optimal geometry of Case 3N

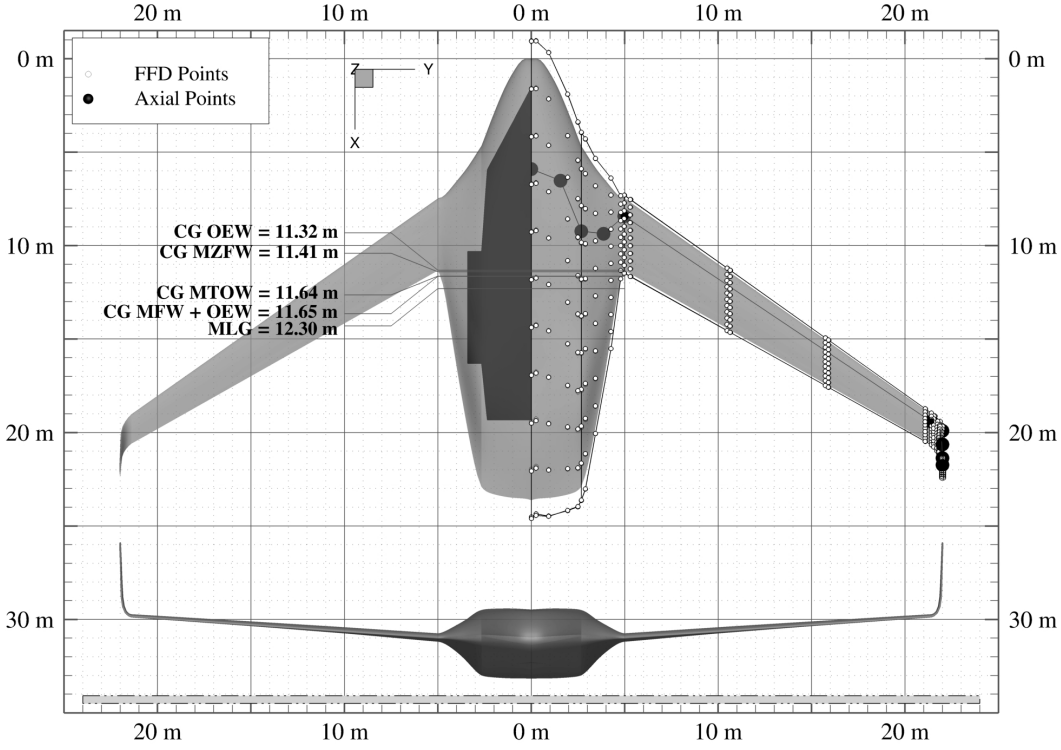

Fig. 3 Optimal geometry of Case 4N

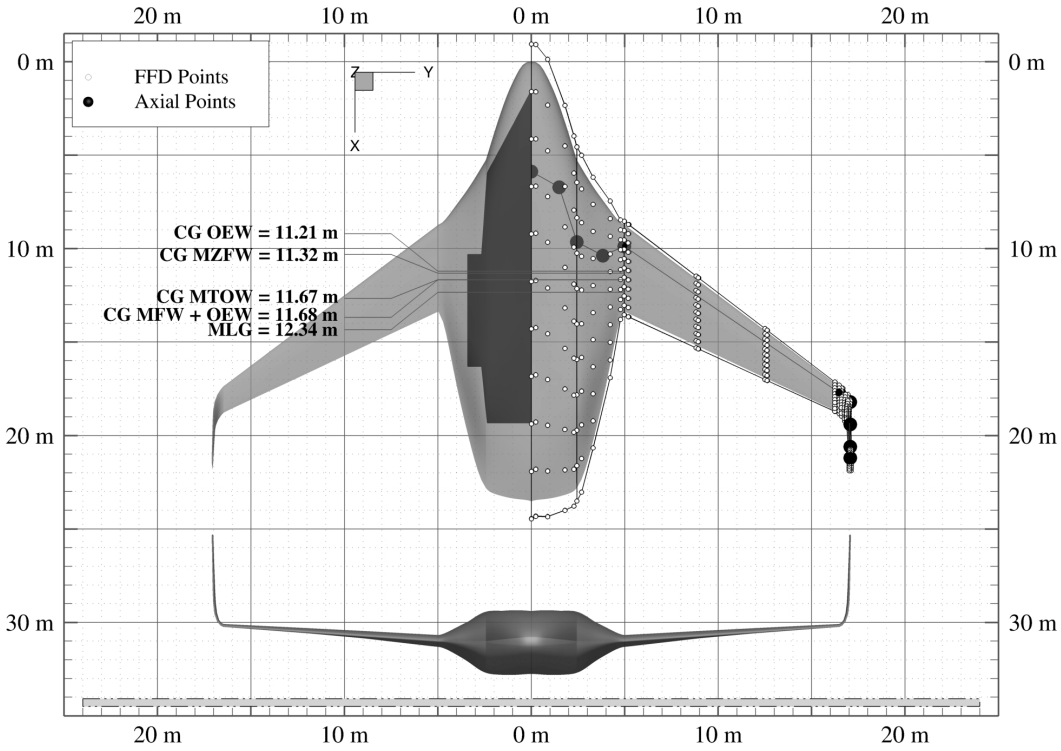

Fig. 4 Optimal geometry of Case $4N_{(R)}$

from significantly degraded performance compared to the equivalent HWB aircraft optimized without imposing the rotation constraint, i.e. Model $4N_{(R)}$. The cruise drag penalty associated with the rotation constraint is 3.8%, that in MTOW is 5.1%, and that in block fuel burn is 4.1%. Geometric adaptations are needed to supplement the pitching moment and are responsible for the large geometric differences between Models 4N and $4N_{(R)}$. Figs. 3 and 4 show the significantly different planforms and front views. The wing root of Model 4N is placed far forward so that the inboard elevon, whose average center of pressure is located ahead of the MLG axles, produces a relatively strong pitching moment about the MLG when deflected downward. A large sweep angle and long wings are then needed to place the outboard elevons and the winglet-mounted rudders well behind the MLG axles. Between Models 4N and $4N_{(R)}$, wingspans differ by 9.86 m. The wings of Model 4N would likely flutter unless they were extremely stiff and therefore heavy. Their span, sweep angle, and wing root position are interdependent and restricted by the tip-strike and dihedral angle constraints. Fortunately, these geometric constraints do not drive the planform in every case, as the wing weight model provides sufficient information on the penalty associated with large spans and sweep angles.

The structural CG perturbation reaches its lower bound of -15.0% in all cases. More precisely, the structural CG is best designed at least 15.0% forward of the position calculated by assuming that the entire aircraft structure is a homogeneous shell except the engines, which are point-masses. To meet this goal in more advanced stages of design, heavy objects could be strategically positioned inside the OML, the engines could be moved slightly forward, and the structural layout could be tailored. The optimizer seeks to move the CG forward through artificial means when no structural CG perturbation is allowed. In such cases, a large drag penalty is typically incurred because the CG is moved forward through the pronounced bulging of the front centerbody. Although this kind of exploitation of the CG definition returns once a bound has been reached, the effect is much reduced. Hence, this structural CG freedom is seen as essential, even though some degree of estimation is involved in the selection of realistic bounds on the design variable. The optimizer can improve performance through such a CG perturbation because it can lengthen the centerbody independently of the CG position (up to the point where a bound has been reached). Therefore, the moment arm of the elevator can be increased with little penalty, and the supplementary pitching moment that is needed once the pitch effectors have been fully relied upon is thus reduced. In addition, the static margin constraints are more readily satisfied when the aircraft is more nose-heavy. This is inherently true, but it is especially important for these HWB aircraft because trimming at low speed with an aft CG can be significantly destabilizing [14].

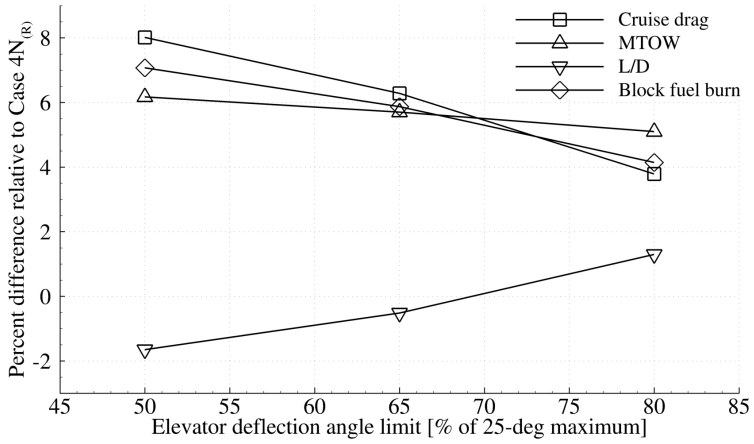

Fig. 5 Variability of design characteristics with elevator deflection angle limit

The interaction between various S&C constraints, which are calculated using different loading conditions, encourages the optimizer to shape the aircraft in such a way that all CGs are close. As shown on Fig. 3, every CG falls within a range of just 0.33 m in Case 4N. The small range of CG locations can be explained by considering that the static margin constraints are more readily satisfied though nose-heaviness but they are calculated at the loading condition corresponding to the aftmost CG. Therefore, it is advantageous to move the aftmost CG as far forward as possible and to design every other CG in close proximity to it in order to minimize trim drag at the cruise analysis point, where the CG is close to that at MTOW, and more readily satisfy the rotation constraint. The result is an aircraft with a CG that would barely move throughout the flight. Hence, trim drag would in fact remain relatively small despite the decreasing fuel load and even without necessarily relying on a fuel management system.

VI. Pitch Effector Deflection Angle Sensitivity Study

A sensitivity study was conducted in order to quantify the performance penalty that would be incurred if a larger margin to pitch effector saturation were desired. The aircraft is reoptimized with elevator deflection angle limits set to 50%, and 65% of the 25° limit. The elevon defection angle limit is maintained at 50%. These two cases are known as $4N_{A1}$ and $4N_{A2}$. They are otherwise identical to Case 4N, which is renamed $4N_{A3}$ in this section only for consistency.

Figure 5 shows the dependence of cruise drag, MTOW, L/D, and block fuel burn on the elevator deflection angle limit. It is clear that favorable design characteristics correlate with increasing elevator deflection angle limit. Taking the cruise drag as an example, the need to supplement the pitching moment through aerodynamically inefficient OML shaping is significantly reduced when the elevator deflection angle limit is increased. It goes from 8.0% with a 50%-deflected elevator to 3.8% with an 80% deflected elevator. Cruise drag is directly reduced through more efficient OML shaping, but this has a compound effect, as it enables a lighter fuel load and induced drag is thus reduced. Consequently, the structural weight is also reduced because the wing, which carries a maximum amount of fuel in every case, can be smaller, so drag is further reduced. These dependencies also lower MTOW and wetted area. The latter quantity is also decreased because the pitch effectors, and by extension the entire aircraft, can be built smaller if the elevator is more effective. For instance, the tip chords of Models $4N_{A1}$ and $4N_{A3}$ are 2.05 m and 1.56 m, respectively, while their root chords and wingspans barely differ. Thus, the lift-to-drag ratio, which depends on the wetted aspect ratio, increases with the elevator deflection angle limit, and block fuel burn decreases. The significant penalty incurred by restricting the use of the elevator motivates the upper bound of 80% used in all studies.

These results appear to have been slightly impacted by multimodality in the design space. Models $4N_{A1}$ and $4N_{A3}$ have almost identical planforms but the wings of Model $4N_{A2}$ are slightly (0.57 m) longer and slightly unswept (32.6° vs. 32.8°). Its centerbody has the lowest mass and the curvature of its upper surface is slightly more pronounced. Hence, it seems that the optimizer may have found two nearby local minima. This hypothesis will be verified in a future study.

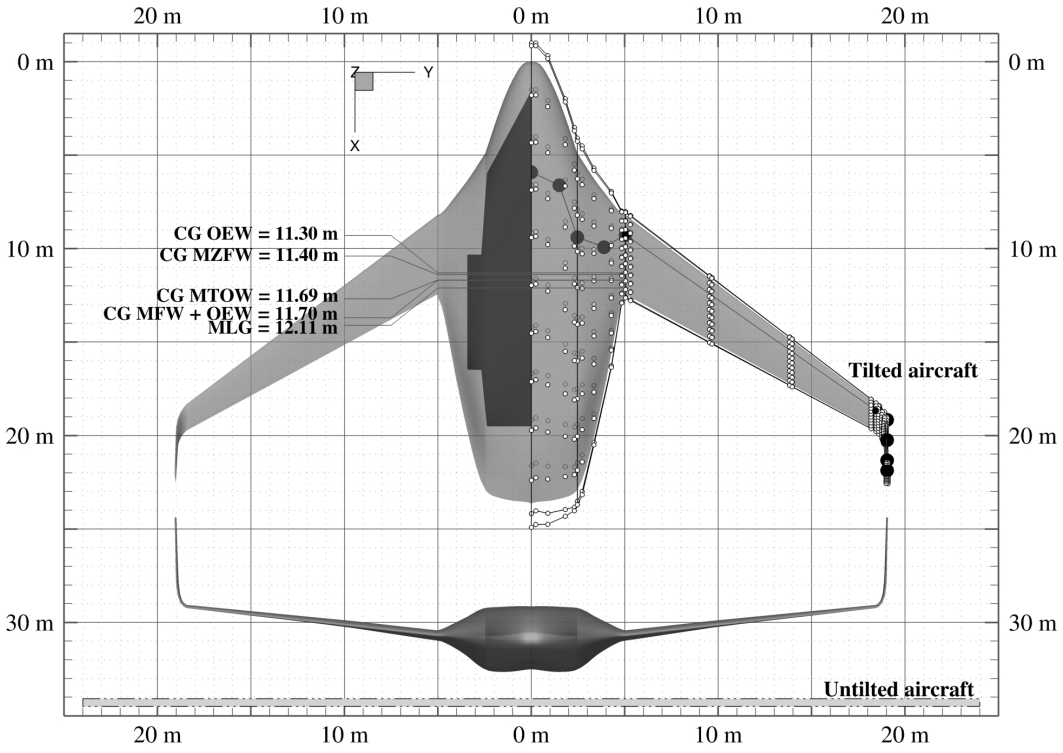

Fig. 6 Optimal geometry of Case $4N_B$

VII. Optimal Cabin Positioning and Telescoping Nose Landing Gear

One limitation of the previous studies is that the OML is optimized around a flat polyhedron fixed in place 5 ft (1.52 m) behind the nose, potentially giving an overly restricted design space. Thus, two new design variables, Δx_c and Δz_c, were implemented to move the polyhedron fore and aft, and up and down, respectively. The resulting changes to the overall CG and mass moment of inertia are also taken into account.

Furthermore, it has been proposed that a telescoping landing gear system could ease the burden of achieving rotation for HWB aircraft [24]. This is a suitable system because the cabin must lie flat at the gate but a tilted aircraft rotates more easily for reasons that are discussed later in this section. The NLG was made telescoping in this study because of the relatively low weight of the required system when compared to telescoping MLG or a combination of telescoping NLG and MLG. The ground-plane remains fixed in the simulation, so the OML must be shaped around a tilted polyhedron to model the effect of telescoping NLG. Therefore, cabin pitch was made variable through a third new design variable, $\Delta\theta \in [0°, 5°]$. The 5° upper bound is half of the angular offset used to position the MLG axles. Finally, the vertical position of the aircraft above the ground-plane is adjusted to reflect the use of telescoping NLG. Ground effect is thus properly modeled. The resulting optimized aircraft is denoted $4N_B$ and is shown in Fig. 6.

The wings are shorter and pushed aft relative to those of Model 4N, and their sweep angle is slightly larger. The effectiveness of the winglet-mounted rudders influences the size and position of the winglets. Therefore, these surfaces grow when the moment arm of the rudders relative to the MLG is shortened in favor of the shorter (and thus lighter) wings. The optimizer determined that maximizing the size of the winglets by making them tall was more favorable than widening the chord at their base. This is because, in this problem definition, the latter option would imply elongating the chords over the entire wing due to its necessarily trapezoidal shape.

The telescoping NLG mechanism is largely responsible for the performance improvement seen here; the Δx_c and Δz_c design variables were barely used (except to accommodate the vertical shift caused by telescoping NLG). The use of telescoping NLG improves performance through at least two mechanisms. First, due to the method used to position the MLG of the untilted aircraft (see Section III.C), the moment arm of the weight vector with respect to the MLG axles is reduced after tilting. Therefore, the *net* pitching moment required to achieve a given pitch acceleration at the start of rotation is reduced. In this case, the moment arm of the weight vector is at most 0.81 m when tilted as opposed to 1.08 m. The punitive contribution of the weight vector to the sum of all pitching moments is therefore reduced by up to 25.1%.

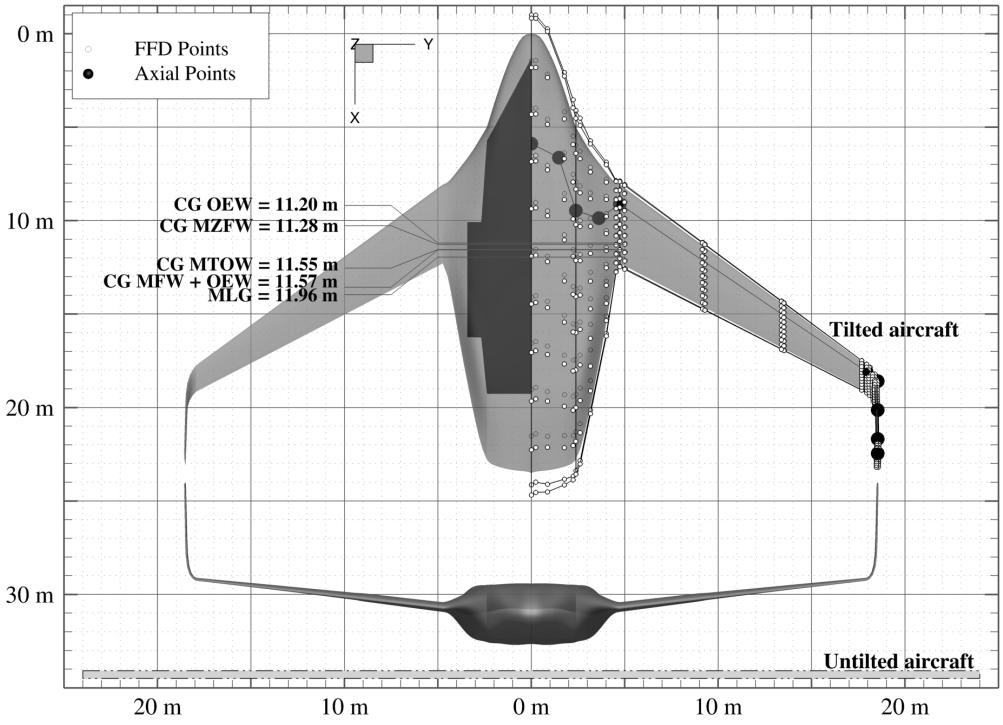

Fig. 7 Optimal geometry of Case $4N_C$

Second, the planform similarities between Models $4N_{(R)}$ and $4N_B$ make it clear that the need to produce a *supplementary* pitching moment after the pitch effectors have been relied upon has been reduced. As shown in Table 1, the net effect is a 3.4% reduction in cruise drag, 3.2% lower MTOW, and 3.3% lower block fuel burn relative to Model 4N.

VIII. Increased Local Shape Control

In Case $4N_C$, the linear interpolation of many sectional design variables is forgone in order to quantify the possible performance benefit. Manufacturing complexity can conceivably be kept nearly constant by considering nonlinearly varying twist angles and section shapes, but one should carefully consider a cost-benefit analysis before considering a nonlinearly tapering wing. Therefore, a nonlinear chord length distribution was not allowed (except on the centerbody, as before). The twist of the winglet remains interpolated; these constraints prevent a number of problems with the mesh deformation algorithm and likely have a relatively small impact on performance. The cabin positioning design variables remain active, and the telescoping NLG model is also used in this case. See Fig. 7 for the optimized geometry.

Despite comprising 398 effective design variables, this case converged in 144 SNOPT major iterations as opposed to 120 for Case $4N_B$, which comprises 173 effective design variables. The results, which are given in Table 1, are a 2.9% improvement in cruise drag, 1.4% lower MTOW, and 2.2% lower block fuel burn relative to Model $4N_B$. Model $4N_C$ also benefits from a 3.5% reduction in wetted area and improved contouring or streamlining of the OML around the inscribed polyhedron. That, combined with the lower weight, can at least partly explain the lower cruise drag.

From the front view in Fig. 8, it is clear that the transition region was blended into the wing with nonlinearly varying section shapes. Moreover, as shown in Fig. 9, this transition region is comparatively well-suited to produce a positive pitching moment for rotation. That of Model $4N_C$ is more fore-loaded and lifting than that of Model $4N_B$. This occurs partly because the section is more twisted, which moves the center of pressure forward if all else remains fixed. Another contributor is the relatively flattened underside of the transition region cross-sections near their leading-edge. This geometric feature is akin to leading-edge carving, which has been previously used to efficiently generate a positive pitching moment [37]. Hence, the optimizer is indeed exploiting the newly unlocked geometric freedom. The nonlinearly distributed twist angles and section shapes also give rise to a local increase in sectional lift in the transition region at cruise, as shown in Fig. 8. The lift distribution is close to elliptical for both Models $4N_B$ and $4N_C$, which attests to their

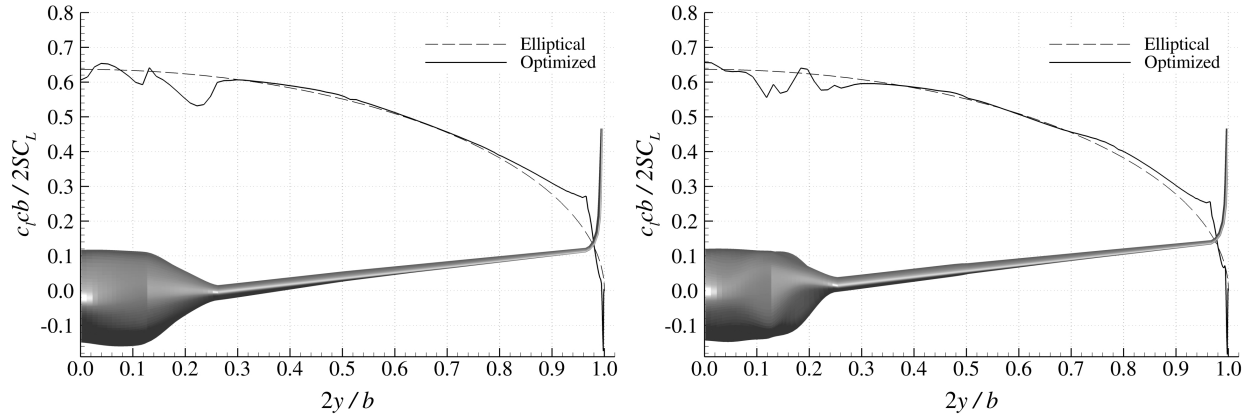

(a) Model 4N$_B$ **(b) Model 4N$_C$**

Fig. 8 Spanwise lift distributions at cruise

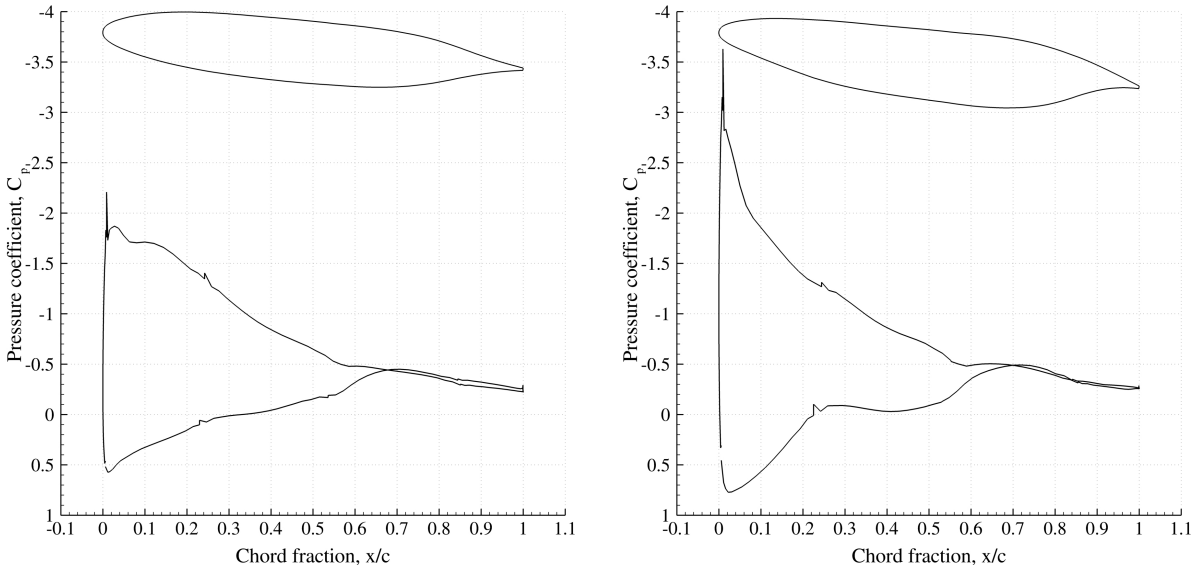

(a) Model 4N$_B$ as tilted by telescoping NLG **(b) Model 4N$_C$ as tilted by telescoping NLG**

Fig. 9 Pressure coefficients at 20% semispan at rotation showing improved pitching moment generation

capability to satisfy the S&C constraints without having an extreme impact on aerodynamic efficiency at cruise.

The optimizer also took advantage of the independent section shape design variables on the wing to construct a thicker root that blends into a thinner mid-section. This moves the CG of the wing and fuel forward, which the optimizer clearly deems beneficial, as the structural CG perturbation reached its forward bound. The optimizer is thus free to shape the rest of the geometry more efficiently.

IX. Conclusions

An exploration of the performance of regional-class HWB aircraft optimized through a multifidelity multidisciplinary optimization framework has been presented. This work expands upon that of Reist et al. [14] through 1) the imposition of low-speed trim and static margin constraints, 2) the development of improved models for the CG location and rotation analysis during the takeoff ground-run, 3) the selection of higher pitch effector deflection angle limits based on a sensitivity study, 4) the explicit modeling of telescoping NLG to assist with rotation, and 5) increased local shape control. With all modifications included, an aircraft was found that produces 15.7% less drag at cruise, has a 5.2% lower

MTOW, and burns 11.2% less fuel during the design mission than that reported in Ref. [14], despite satisfying the additional low-speed trim and static margin constraints. Its cruise lift-to-drag ratio of 22.8 and its nearly elliptical cruise lift distribution also attest to its relatively high aerodynamic efficiency. Finally, its relatively low MTOW of 46 700 kg makes it comparable to existing conventional regional-class aircraft with MTOWs in the 45 300 kg to 52 200 kg range.

In order to better understand the relative performance of regional-class HWB aircraft, future work could include the optimization of regional-class conventional tube-and-wing aircraft using the same S&C-constrained framework. In addition, fins have been proposed as an alternative means of achieving directional stability and control for HWB aircraft [14]. In cases with an elongated and relatively narrow centerbody, it is conceivable that this could lead to further performance benefits because the position of the wingtips would be decoupled from the directional control requirement. Finally, additional avenues exist for increasing the geometric freedom, the most prominent of which is the design of elevons with unequal span fractions. Another option is the exploration of wings with nonlinearly distributed chord lengths while employing an appropriate weight model.

Appendices

Appendix A. Operating Conditions at the Various Analysis Points

The following operating conditions are used to analyze the HWB aircraft at cruise, on the ground with one engine inoperative, at the start of rotation, and while flying level at low-speed and altitude.

1) Start of cruise
   - Speed: Cruise speed, Mach 0.78
   - Altitude: Cruise altitude, 36 000 ft (10 973 m)
   - Controls: No deflections allowed
   - Weight: Start of cruise, where taxi, takeoff, and climb fuel has been spent
   - CG: Unperturbed and corresponding to a typical fuel situation at the start of cruise (except the untrimmed static margin constraint is calculated with the aftmost CG)
   - Thrust: Horizontal component set equal to cruise drag
2) One engine inoperative (OEI) on the ground
   - Speed: Target minimum control speed on the ground $\in$ [Mach 0.1, Mach 0.2]
   - Altitude: Sea-level with a moving ground-plane
   - Controls: Full rudder deflections allowed (±30°)
   - Weight: Conservative OEW estimate, 95% OEW, to check that rudders do not cause rotation
   - CG: Conservatively perturbed rearward, by 2.5% l_{ref}, to check that rudders do not cause rotation
   - Thrust: Conservative estimate of OEI thrust taken to be equal to half of the total sea-level static thrust
3) Start of rotation
   - Speed: Target rotation speed $\in$ [Mach 0.1, Mach 0.2]
   - Altitude: Sea-level with a moving ground-plane
   - Controls: Elevator allowed to deflect up to 80% (±20°); elevons allowed to deflect up to 50% (±12.5°)
   - Weights: MTOW, MZFW, OEW + MFW, and OEW; each loading condition is analyzed
   - CG: Conservatively perturbed forward by 2% l_{ref} at the MTOW, MZFW, and OEW + MFW loading conditions, and by 3.5% l_{ref} at OEW
   - Thrust: Conservative estimate of rotation thrust taken to be equal to the sea-level static thrust
4) Low-speed flight at low altitude
   - Speed: Low-speed flight, Mach 0.20
   - Altitude: Free air at sea-level
   - Controls: Elevator allowed to deflect up to 80% (±20°); elevons allowed to deflect up to 50% (±12.5°)
   - Weight: OEW + MFW; corresponding to the heaviest aft CG (which is the aftmost in all relevant cases)
   - CG: Aftmost CG among the MTOW, MZFW, OEW + MFW, and OEW loading conditions
   - Thrust: Conservatively assumed to be zero in case a total engine failure occurs

Appendix B. Full Dataset

Table 2 is an extension of Table 1 showing, for instance, a more complete weight breakdown and the values of relevant geometric inequality constraints. It can be used to compare performance and identify the design choices that drive the optimal geometry.

Table 2 Characteristics and performance of optimal shapes

	3N	4N	$4N_{(R)}$	$4N_B$	$4N_C$
Performance and S&C constraints [*]					
Cruise drag [kN]	20.29	20.75	19.99	20.04	19.45
Cruise drag coefficient [counts]	81.54	82.48	88.35	84.95	86.77
Block fuel burn [kg]	7 040	7 160	6 880	6 920	6 770
Cruise L/D	22.75	22.44	22.15	22.49	22.83
Cruise C_L	0.1855	0.1851	0.1957	0.1911	0.1981
Cruise K_n [% l_{ref}]	-3.78	-1.10	-0.357	-0.988	-0.964
Cruise K_n, aft CG [% l_{ref}]	**-4.00**	-1.38	-0.778	-1.34	-1.37
Low-speed K_n [% l_{ref}]	N/A	**-4.00**	**-4.00**	**-4.00**	**-4.00**
Pitch acceleration [deg/s^2]	**3.00**	**3.00**	N/A [†]	**3.00**	**3.00**
Loading condition weight data					
MTOW [kg]	48 600	49 000	46 600	47 400	46 700
MZFW [kg]	39 000	39 200	37 300	38 000	37 500
MFW + OEW [kg]	38 400	38 800	36 400	37 200	36 500
OEW (incl. fixed weights) [kg]	28 800	29 000	27 100	27 800	27 300
Body [kg]	10 300	10 300	9 660	9 810	9 610
Wings / winglets [kg]	4 370 / 156	4 570 / 172	3 280 / 195	3 850 / 186	3 640 / 202
Propulsion [kg]	3 080	3 140	3 030	3 050	2 980
Key geometric data and constraints [*]					
Span [m]	41.39	43.98	34.12	38.06	37.05
Excess centerbody span [m]	0.523	0.619	0.142	0.192	0.038
Planform area [m^2]	255.3	258.1	232.1	241.9	230.0
Wetted area [m^2]	584.2	593.4	543.0	562.3	542.4
Wetted aspect ratio	2.932	3.260	2.144	2.577	2.531
Cruise deck angle [deg]	1.38	1.53	**2.50**	**2.50**	**2.50**
Wing dihedral angle [deg]	**4.00**	**4.00**	3.99	6.38	6.46
Wing sweep [deg]	39.4	33.7	34.2	35.0	33.8
Winglet sweep [deg]	**30.0**	**30.0**	35.0	34.8	41.1
Winglet aspect ratio	3.11	3.04	**4.00**	3.68	3.88
Tip-strike margin [m]	**0.00**	**0.00**	0.772	1.38	1.52
Excess ground clearance [m]	**0.00**	**0.00**	0.348	0.157	0.140
Excess wing volume [m^3]	**0.00**	**0.00**	**0.00**	**0.00**	**0.00**
Cabin clearance [m]	**0.00**	**0.00**	**0.00**	**0.00**	**0.00**
Structural CG perturbation [%]	**-15.0**	**-15.0**	**-15.0**	**-15.0**	**-15.0**

[*] Boldface indicates constraint activity.
[†] This constraint was not imposed but $\ddot{\theta} = -6.04\,\text{deg/s}^2$ at the most critical loading condition (MZFW in this case).

Acknowledgments

The authors wish to thank the University of Toronto and the Natural Sciences and Engineering Research Council of Canada for their financial support. Computations were performed on the Niagara supercomputer at the SciNet HPC Consortium. SciNet is funded by: the Canada Foundation for Innovation under the auspices of Compute Canada, the Government of Ontario, the Ontario Research Fund - Research Excellence, and the University of Toronto.

References

[1] "Aircraft Technology Roadmap to 2050," Tech. Rep., International Air Transport Association, Dec. 2019.

[2] Greitzer, E. M., Bonnefoy, P. A., Hall, D. K., Hansman, R. J., Hileman, J. I., Liebeck, R. H., Lovegren, J., Mody, P., Pertuze, J. A., Sato, S., Spakovszky, Z. S., Tan, C. S., Hollman, J. S., Duda, J. E., Fitzgerald, N., Houghton, J., Kerrebrock, J. L., Kiwada, G. F., Kordonowy, D., Parrish, J. C., Tylko, J., and Wen, E. A., "N+3 Aircraft Concept Designs and Trade Studies, Final Report," Tech. Rep. NASA/CR-2010-216794/VOL1, National Aeronautics and Space Administration, Cleveland, Ohio, U.S.A., Dec. 2010.

[3] Gagnon, H., and Zingg, D. W., "Euler-Equation-Based Drag Minimization of Unconventional Aircraft Configurations," *Journal of Aircraft*, Vol. 53, No. 5, 2016, pp. 1361–1371. doi:10.2514/1.C033591.

[4] Faggiano, F., Vos, R., Baan, M., and Van Dijk, R., "Aerodynamic Design of a Flying V Aircraft," *17th AIAA Aviation Technology, Integration, and Operations Conference*, American Institute of Aeronautics and Astronautics, Paper 2017-3589, Denver, Colorado, USA, 2017. doi:10.2514/6.2017-3589.

[5] Callaghan, J. T., and Liebeck, R. H., "Some Thoughts on the Design of Subsonic Transport Aircraft for the 21st Century," *Aerospace Technology Conference and Exposition*, Society of Automotive Engineers, Paper 901987, Long Beach, California, USA, 1990. doi:10.4271/901987.

[6] Liebeck, R. H., "Design of the Blended Wing Body Subsonic Transport," *Journal of Aircraft*, Vol. 41, No. 1, 2004, pp. 10–25. doi:10.2514/1.9084.

[7] Okonkwo, P., and Smith, H., "Review of evolving trends in blended wing body aircraft design," *Progress in Aerospace Sciences*, Vol. 82, 2016, pp. 1–23. doi:10.1016/j.paerosci.2015.12.002.

[8] "Airbus reveals its blended wing aircraft demonstrator," Document, Airbus Media Relations, Feb. 2020.

[9] Qin, N., Vavalle, A., and Le Moigne, A., "Spanwise Lift Distribution for Blended Wing Body Aircraft." *Journal of Aircraft*, Vol. 42, No. 2, 2005, pp. 356–365. doi:10.2514/1.4229.

[10] Peigin, S., and Epstein, B., "Computational Fluid Dynamics Driven Optimization of Blended Wing Body Aircraft," *AIAA Journal*, Vol. 44, No. 11, 2006, pp. 2736–2745. doi:10.2514/1.19757.

[11] Kuntawala, N., Hicken, J., and Zingg, D., "Preliminary Aerodynamic Shape Optimization of a Blended-Wing-Body Aircraft Configuration," *49th AIAA Aerospace Sciences Meeting including the New Horizons Forum and Aerospace Exposition*, American Institute of Aeronautics and Astronautics, Paper 2011-642, Orlando, Florida, USA, 2011. doi:10.2514/6.2011-642.

[12] Méheut, M., Arntz, A., and Carrier, G., "Aerodynamic Shape Optimizations of a Blended Wing Body Configuration for Several Wing Planforms," *30th AIAA Applied Aerodynamics Conference*, American Institute of Aeronautics and Astronautics. Paper 2012-3122, New Orleans, Louisiana, USA, 2012. doi:10.2514/6.2012-3122.

[13] Mader, C. A., and Martins, J. R. R. A., "Stability-Constrained Aerodynamic Shape Optimization of Flying Wings," *Journal of Aircraft*, Vol. 50, No. 5, 2013, pp. 1431–1449. doi:10.2514/1.C031956.

[14] Reist, T. A., Zingg, D. W., Rakowitz, M., Potter, G., and Banerjee, S., "Multifidelity Optimization of Hybrid Wing–Body Aircraft with Stability and Control Requirements," *Journal of Aircraft*, Vol. 56, No. 2, 2019, pp. 442–456. doi:10.2514/1.C034703.

[15] Lyu, Z., and Martins, J. R. R. A., "Aerodynamic Design Optimization Studies of a Blended-Wing-Body Aircraft," *Journal of Aircraft*, Vol. 51, No. 5, 2014, pp. 1604–1617. doi:10.2514/1.C032491.

[16] Vicroy, D., "Blended-Wing-Body Low-Speed Flight Dynamics: Summary of Ground Tests and Sample Results (Invited)," *47th AIAA Aerospace Sciences Meeting and Exhibit*, American Institute of Aeronautics and Astronautics, Paper 2009-0933, Orlando, Florida, USA, 2009. doi:10.2514/6.2009-933.

[17] Cook, M. V., and de Castro, H. V., "The longitudinal flying qualities of a blended-wing-body civil transport aircraft," *The Aeronautical Journal*, Vol. 108, No. 1080, 2004, pp. 75–84. doi:10.1017/S0001924000005029.

[18] Garmendia, D. C., Chakraborty, I., and Mavris, D. N., "Method for Evaluating Electrically Actuated Hybrid Wing–Body Control Surface Layouts," *Journal of Aircraft*, Vol. 52, No. 6, 2015, pp. 1780–1790. doi:10.2514/1.C033061.

[19] Wakayama, S., "Multidisciplinary design optimization of the blended-wing-body," *Proceedings of the 7th AIAA/USAF/NASA/ISSMO Symposium on Multidisciplinary Analysis and Optimization*, American Institute of Aeronautics and Astronautics, St. Louis, Missouri, USA, 1998. doi:10.2514/6.1998-4938.

[20] Wakayama, S., "Blended-wing-body optimization problem setup," *8th Symposium on Multidisciplinary Analysis and Optimization*, American Institute of Aeronautics and Astronautics, Paper 2000-4740, Long Beach, California, USA, 2000. doi:10.2514/6.2000-4740.

[21] Morris, A., "MOB A European Distributed Multi-Disciplinary Design and Optimisation Project," *9th AIAA/ISSMO Symposium on Multidisciplinary Analysis and Optimization*, American Institute of Aeronautics and Astronautics, Paper 2002-5444, Atlanta, Georgia, USA, 2002. doi:10.2514/6.2002-5444.

[22] Hileman, J. I., Spakovszky, Z. S., Drela, M., Sargeant, M. A., and Jones, A., "Airframe Design for Silent Fuel-Efficient Aircraft," *Journal of Aircraft*, Vol. 47, No. 3, 2010, pp. 956–969. doi:10.2514/1.46545.

[23] Reist, T. A., and Zingg, D. W., "High-Fidelity Aerodynamic Shape Optimization of a Lifting-Fuselage Concept for Regional Aircraft," *Journal of Aircraft*, Vol. 54, No. 3, 2017, pp. 1085–1097. doi:10.2514/1.C033798.

[24] Yang, S., Page, M., and Smetak, E. J., "Achievement of NASA New Aviation Horizons N+2 Goals with a Blended-Wing-Body X-Plane Designed for the Regional Jet and Single-Aisle Jet Markets," *2018 AIAA Aerospace Sciences Meeting*, American Institute of Aeronautics and Astronautics, Paper 2018-0521, Kissimmee, Florida, USA, 2018. doi:10.2514/6.2018-0521.

[25] Koo, D., and Zingg, D. W., "Investigation into Aerodynamic Shape Optimization of Planar and Nonplanar Wings," *AIAA Journal*, Vol. 56, No. 1, 2018, pp. 250–263. doi:10.2514/1.J055978.

[26] Gagnon, H., and Zingg, D. W., "Two-Level Free-Form and Axial Deformation for Exploratory Aerodynamic Shape Optimization," *AIAA Journal*, Vol. 53, No. 7, 2015, pp. 2015–2026. doi:10.2514/1.J053575.

[27] Hicken, J. E., and Zingg, D. W., "Aerodynamic Optimization Algorithm with Integrated Geometry Parameterization and Mesh Movement," *AIAA Journal*, Vol. 48, No. 2, 2010, pp. 400–413. doi:10.2514/1.44033.

[28] Osusky, M., Boom, P. D., and Zingg, D. W., "Results from the Fifth AIAA Drag Prediction Workshop obtained with a parallel Newton-Krylov-Schur flow solver discretized using summation-by-parts operators," *31st AIAA Applied Aerodynamics Conference*, American Institute of Aeronautics and Astronautics, Paper 2013-2511, San Diego, California, USA, 2013. doi:10.2514/6.2013-2511.

[29] Osusky, M., and Zingg, D. W., "Parallel Newton–Krylov–Schur Flow Solver for the Navier–Stokes Equations," *AIAA Journal*, Vol. 51, No. 12, 2013, pp. 2833–2851. doi:10.2514/1.J052487.

[30] Torenbeek, E., "8.4.1 - Airframe Structure," *Synthesis of Subsonic Airplane Design*, Springer Science+Business Media, B.V., Dordrecht, 1982, 1st ed., pp. 277–285.

[31] Gill, P. E., Murray, W., and Saunders, M. A., "SNOPT: An SQP Algorithm for Large-Scale Constrained Optimization," *SIAM Journal of Optimization*, Vol. 12, No. 4, 2002, pp. 979–1006. doi:10.1137/S0036144504446096.

[32] Hicken, J. E., and Zingg, D. W., "A Simplified and Flexible Variant of GCROT for Solving Nonsymmetric Linear Systems," *SIAM Journal on Scientific Computing*, Vol. 32, No. 3, 2010, pp. 1672–1694. doi:10.1137/090754674.

[33] Osusky, L., Buckley, H., Reist, T., and Zingg, D. W., "Drag Minimization Based on the Navier–Stokes Equations Using a Newton–Krylov Approach," *AIAA Journal*, Vol. 53, No. 6, 2015, pp. 1555–1577. doi:10.2514/1.J053457.

[34] Green, J. E., "Civil aviation and the environment – the next frontier for the aerodynamicist," *The Aeronautical Journal*, Vol. 110, No. 1110, 2006, pp. 469–486. doi:10.1017/S0001924000001378.

[35] Mukhopadhyay, V., and Sorokach, M. R., "Composite Structure Modeling and Analysis of Advanced Aircraft Fuselage Concepts," *AIAA Modeling and Simulation Technologies Conference*, American Institute of Aeronautics and Astronautics, Paper 2015-3096, Dallas, Texas, USA, 2015. doi:10.2514/6.2015-3096.

[36] Roskam, J., "2.5.3 - Mathematical Model for Analyzing Control During the Takeoff Groundrun," *Airplane Design, Part VII: Determination of Stability, Control and Performance Characteristics: FAR and Military Requirements*, Design, Analysis and Research Corporation, Lawrence, Kansas, USA, 1989, 1st ed., pp. 36–44.

[37] Sargeant, M. A., Hynes, T. P., Graham, W. R., Hileman, J. I., Drela, M., and Spakovszky, Z. S., "Stability of Hybrid-Wing-Body-Type Aircraft with Centerbody Leading-Edge Carving," *Journal of Aircraft*, Vol. 47, No. 3, 2010, pp. 970–974. doi:10.2514/1.46544.